Ice Sheet Motion and Topography from Radar Interferometry

R. Kwok, M. Fahnestock* and C. Chan

Jet Propulsion Laboratory
California Institute of Technology
4800 Oak Grove Drive
Pasadena, CA 91109

* *Goddard Space Flight Center*
Greenbelt, MD

Submitted to *IEEE TGARS*

September 22, 1994

Please send correspondences to:

Dr. Ronald Kwok
Jet Propulsion laboratory
California Institute of Technology
MS 300-235
4800 Oak Grove Drive
Pasadena, CA 91109

ICE SHEET MOTION AND TOPOGRAPHY FROM RADAR INTERFEROMETRY

R. Kwok, M. Fahnestock* and C. Chan

Jet Propulsion Laboratory
California Institute of Technology
Pasadena, CA 91109

**Goddard Space Flight Center*
Greenbelt, MD

Abstract

Both topography and motion information are present in repeat pass ERS-1 interferograms over ice sheets. We demonstrate that the topography is separable from the surface displacement field when a sequence of of radar images are available. If the velocity field is constant over the time span of observation, the topography can be derived from differential interferograms formed from sequential observations. With this measurement, a pure displacement field can then be obtained by removal of the topographic contribution to the interferometric phase at each pixel. Further, we discuss how the vertical and horizontal components of displacement affect the interferometrically-derived motion field. We illustrate our approach with four successive (3-day repeat) ERS-1 images of a flow feature in northeastern Greenland.

1 Introduction

The potential of using satellite radar interferometry (SRI) to monitor ice flow velocities and grounding-line positions of ice streams was first discussed in Goldstein et al. [1]. In their study, interferometric data over the Rutford Ice Stream, Antarctica was used to illustrate the capabilities of SRI and the derived information were compared with available surface observations. Recently, Joughin et al. [2] discussed the complexity of the fringe patterns in western Greenland using a 100km x 500km strip of ERS-1 (European Earth Remote Sensing Satellite) interferogram stretching from the interior of the ice sheet to the western coast of Greenland. Both investigators have observed that the fringe patterns are expressions of ice motion and surface topography. Joughin et al. also noted that the motion fringes can be decomposed into vertical and horizontal components if the displacements conform to surface relief. The contributions of two components to the observed line of sight motion is dependent on the look angle and surface slopes, At steep look angles, like that of ERS- 1, the vertical component is exaggerated compared to the horizontal component. The separation of the topographic and motion contributions to the interferometric phase is essential to the interpretation of such fringe patterns, especially if the interferometric baseline is significant. However, surface topography at the spatial scale which affects fringe patterns is typically not available over ice sheets.

In this paper, we demonstrate that if the ice flow velocity is constant over the period of observation, both motion and surface relief information can be extracted using multiple pass interferometric analysis. The focus of our analysis is on a flow feature in northeast Greenland described by Fahnestock et al. [3]. A series of four ERS- 1 images spaced every three days was used to generate mixed motion/topography interferograms with 3-, 6- and 9-day separations. The procedure of separating motion from topography involves first differencing two 3-day interferograms to remove the motion contributions leaving fringe patterns solely due to surface relief. These topographic fringe patterns can then be removed from a 6-day interferogram to isolate the motion fringes. The technique and its application are described in more detail in the following six sections. The Synthetic Aperture Radar (SAR) dataset used in this analysis is described in Section 2. Section 3 covers the procedure used to form the interferograms from complex SAR data with a brief description of the expected errors and sensitivities. We describe our approach to extract tile topography-only interferogram using differential interferometry is described in Section 4. With this derived surface relief, Section 5 discusses the method we used to remove the topographic contributions to the fringe patterns and the effect of surface slope on the observed displacement field. The observed flow field is briefly discussed in Section 6. Discussion of the implications of SRI for measurement of ice sheet topography and monitoring of flow velocities and patterns is provided in the last section.

2 Data Description

The four SAR images used here were processed at the German ERS- 1 processing and archive facility (D-PAF) in Oberpfaffenhofen, Germany. These images were acquired in the early part of January of 1994 and received at the Kiruna station. Table 1 shows the orbit/frame numbers and dates of acquisition of these images. The location of the images on Greenland are shown in Fig. 1. We obtained single-look, complex, slant-range data with the product designation of *ERS-1.SAR.SLC* for our interferometric analysis. For this particular product type, each 100km by 100km image frame is divided into four quadrants each with **2500** complex samples in the range direction and bet.ween 14000 and 15000 lines in the azimuth direction. The real (1) ant] imaginary (Q) part of each sample is represented by a 2-byte signed integer. The near range and far range quadrants have a fixed overlap of 88 samples, The azimuth overlap is variable but is approximately 3000 samples. The processed data have been yaw-steered to zero Doppler such that wc do not expect any residual phase function to affect our results. The spatial resolutions arc approximately 11 m and 1 Om in the slant range and azimuth directions, respectively. '1'here is a 3-day period between successive observations of this flow feature in Greenland. Since two range quadrants from the four days covered most of the flow feature, we mosaicked only these range quadrants to obtain a c.overage of 55km by 1001in) in azimuth and range directions, respectively.

3 Ice Sheet Interferometry

The theory and techniques for radar interferometry have been presented in detail elsewhere [4, 5,6, i']. Also, a recent article by Zebker et al. [8] has discussed the accuracy of topographic maps derived from ERS-1 repeat pass interferometry. Of particular interest is the application of differential interferometry [9] to map small displacements over large areas. We will be using differential interferometry, however, to analyze a slightly different- problem. The reader is referred to these articles for background on radar interferometry. The brief description provided here serves as a review of the technique and establishes the notation used throughout the paper. Here, we will attempt to be comprehensive but our focus is on the issues associated with the application of radar interferometry to the remote sensing of ice sheets.

3.1 *Review* ant] Notation

In this paper, we discuss ice motion in terms of the following quantities: position, displacement and velocity. Consider an ice particle on the ice sheet at a position X at time t_0; at some later time the ice particle has moved to a new position $\mathbf{x}(t; X)$. A displacement is the finite difference in the positions of an ice particle at two different times,

$$\mathbf{u} = \mathbf{x}(t_2) - \mathbf{x}(t_1).$$

The average velocity over the time interval $\Delta T = t_2 - t_1$ is,

$$\mathbf{v} = \mathbf{u}/\Delta T.$$

We assume that the displacement field is spatially slowly varying such that tile velocity is meaningful in this context.

The coordinate system and geometry for multiple-observation interferometry is depicted in Fig. 2. For a given set of repeat observation, from the ith and jth epochs, with baseline B_{ij} and look angle θ, the phase difference at each sample is

$$\Delta\phi_{ij} = \frac{4\pi}{\lambda} B_{ij} sin(\theta - \alpha_{ij})$$

where α is the tilt of the baseline with respect to the horizontal. If the scatterers are displaced by $\Delta\rho$ in range then the observed phase will include a contribution of $\frac{4\pi}{\lambda}\Delta\rho$ clue this displacement, or

$$\Delta\phi_{ij} = \frac{4\pi}{\lambda} B_{ij} sin(\theta - \alpha_{ij}) + \frac{4\pi}{\lambda}\Delta\rho \tag{1}$$

We note here that this additional term is independent of the spatial baseline. The phase due to the displacement field is not scaled by this baseline. However, as we discuss later, it is sensitive to the temporal baseline for a smooth velocity field.

The approximate baseline, B_{ij} at their image centers, between each pair of images is shown in 'J'able 2 [10]. The actual baselines vary slightly along track, We show the values to give the reader an indication of the magnitude and variation of the baselines when using ERS- 1 as a repeat-pass interferometric radar. In the table, the baselines arc decomposed into a component which is perpendicular to the line of sight or range direction $(B_{\perp} = B cos(\theta - \alpha))$ and a component which is parallel to this direction $(B_{\parallel} = B sin(\theta - \alpha))$. The sensitivity of the interferometer to surface relief is dependent on the magnitude of this perpendicular separation.

3.2 Generation of Interferograms

The two steps we follow in interferometric processing arc: registration of the SAR images; and, formation of the multi-look interferogram. To register the SAR images, wc must first determine the spatial misregistration between images. Typically, the largest contribution to image misregistration is offset clue to uncertainty in sensor location. There is slight misregistration in the range direction clue to the difference in the look angle between repeat passes. Further, slight azimuth dependent misregistration can be caused by diverging or converging orbit tracks. The procedure we use: to determine subpixel offset corrections is based on visibility of the fringes in an interferogram [] I]. Wc select sixty-four windows of size 9 x 9 samples uniformly distributed over the first image. Starting with an approximate location on the second image, wc multiply onc of these windows from the first image with the complex conjugate of a window of the same size on the second image to form an initial fringe pattern. A two-dimensional fast Fourier transform (FFT) is then performed on this product array to obtain a two-dimensional fringe spectrum. The peak value (complex absolute value) in the spectrum represents the two spatial frequencies f_x and f_y at which the brightest fringes at that location arc observed. This peak value is recorded. The window is shifted in a two dimensional grid (16 x 16) to obtain an array of peak values, the maximum of which gives the location of registration. Subpixel offsets are obtained by quadratic interpolation of a 3 x 3 subwindow centered around the maximum of this sampled array. The procedure is repeated for each of the windows extracted from the first image. Once the Offset f or each window is determined, a quadratic surface is fitted to the offsets and one of the images is resampled into the grid of the other image to bring it into almost exact (typically to better than an eighth of a pixel) registration.

The next step is to form the multilook interferogram by first multiplying one image with the complex conjugate of the second image. To reduce the phase noise at each sample, wc average the complex samples over 4 samples in the range direction and 12 samples in the azimuth direction (this process is usually referred to as multi-looking), after whit]) the estimated interferometric phase at each sample is given by,

$$\hat{\Phi} = tan^{-1}\left(\frac{Im\sum v_1 v_2^*}{Re\sum v_1 v_2^*}\right)$$

where the sum is over the 4 x 12 complex samples of the product interferometric image giving us approximately 20 independent samples. We have less than 48 independent samples because the samples are correlated. It has been shown [7] that $\hat{\Phi}$ computed in this manner gives the maximum likelihood estimate of the interferometric phase. The resultant phase noise after this averaging process is dependent on baseline decorrelation and the signal-to-noise ratio (SNR) of the data assuming no temporal decorrelation between datatakes. Baseline decorrelation results from viewing the surface at two slightly different look angles and increases with increasing baseline. Referring to Fig. 2 in Zebker [8] and assuming a baseline of 80m and a SNR of 10dB, wc expect the phase noise to be, conservatively, better than 100. Increasing the number of samples used in the averaging process would decrease the phase noise, but at the expense of resolution. A final correction is made to the phase at each pixel to remove the estimated phase shift that results from the slightly different positions of the spacecraft when the radar data for the two images were obtained. In other words, wc remove the phase function due to observation of a spherical surface from two points so as to emphasize the motion and surface relief,

3.3 Repeat-pass interferograms

The relatively featureless El{, S-l SAR image of the flow feature is shown in Fig. 3. Six different interferograms were formed from the image sequence over the flow feature in Greenland, three of which arc shown in Fig. 4. Each interferogram shows the phase shift at each pixel relative to the first image. In our color coding scheme, a 2π phase shift is represented by a cycle of the color wheel (increasing in the direction from yellow-red-blue- green-yc]low). The phase shift is a measure of the varying topography on the icc sheet as wel] as the range displacement of the surface during the repeat observation interval. As noted above, the fringe patterns due to topography arc sensitive the the baseline of the interferometer whereas those due to range displacements arc not. For a typical ERS- 1 baseline of say 80m, the sensitivity to topography is approximately 2001n/fringe, Half a wavelength of range displacement (2.8 cm for 101{. S- 1 radar wavelength of 5.6 cm) produces a phase shift of 5.6 cm. If we assume no surface relief (or zero baseline), each fringe can be converted to a horizontal surface velocity of $2.8/(\Delta T \sin\theta)$ cm/day in the range direction where θ is the look angle and ΔT is the time separation between the images in days. We discuss the effect of surface relief on this horizontal velocity in a later section. At the nominal ERS-1 look angle of 23° and a ΔT = 3 days, this quantity is approximately 2.4 cm/day or 8.7 m/year. With the magnitude of phase noise (10°) from the above discussion, the statistical uncertainty in topography and motion due to phase noise are approximately 5m (with this baseline) and 0.07 cm/day, respectively. These are the limits of observation. Increasing the time separation, or temporal baseline, would reduce the uncertainty in the motion observation. We note here that the zero of the phase shift is arbitrary, and absolute motion can be determined only if a reference target is available. Consequently, only relative motion can be obtained in the absense of such a target. To approach these limits in the estimation of absolute topography and motion requires very accurate knowledge of the baseline and position of the interferometer during the data acquisition. Long wavelength residuals in the derived topography are inherent in the interferograms, even with very accurate baselines. An alternative is to use tiepoints to provide elevation references in the interferometric analysis. A detailed account of ERS-1 interferometer performance using elevation tiepoints was provided by Zebker [8] and will not be repeated here. However, visual tiepointing might not work over the featureless ice sheet; we shall return to this discussion later in this paper. It is important to realize that without accurate ephemeris or tiepoints, in a relative sense, the topographic or motion maps are quite accurate because these systematic errors introduce only a slowly varying bias to each pixel. We shall address only relative height measurements and relative motion in the balance of this paper.

The motion due to the flow feature is clearly seen in multiple-pass interferograms. As expected, the fringe rate increases proportionately with the time separation between the images used in the interferometric analysis. Proceeding from the top left to the bottom right of one of the images, we see that the velocity increases as we cross one margin toward the middle of the ice stream and then decreases across the other margin. The visibility of the fringes is very good in all the interferograms. There is a slight temporal dependence in the correlation coefficients in the areas with relatively few fringes. We observe an expected correlation coefficient of between 0.7 and 0.8 [see 8] in the 3-clay interferograms with a decrease to between 0.6 and 0.7 m the 9-day interferograms. We do not explain the source of the observed temporal decorrelations in this papern although the greatest decorrelation occur-s in high strain regions, as would be expected. We leave this as a topic for future investigations. The discussion of the flow of the ice feature is given in Section 6.

4 Topography from Differential Interferometry

The fringe patterns in Fig. 4 contain the combined effects of topography and ice motion. '1'0 obtain a true motion field, the contribution of topography to the phase of each pixel has to be removed. Our approach is to utilize differential interferometry in this analysis. Gabriel et al. [1 1] first used differential interferometry to detect small displacements. The procedure involves scaling the baselines and differencing the two interferograms to detect changes in the fringe patterns. The scaling normalizes each interferogram with its own baseline such that the phase measurements arc on identical scales before the differencing process. We contrast their objective, detecting changes relative to a reference interferogram, to ours, which is to separate ice motion fringe patterns from fringe patterns due to topography.

Consider the phase from two interferograms from three passes (images 1, 2 and 3) over the i ce feature,

$$\begin{aligned}
\Delta\phi_{12} &= \frac{4\pi}{\lambda} B_{12} sin(\theta - \alpha_{12}) + \frac{4\pi}{\lambda}\Delta\rho \\
\Delta\phi_{23} &= \frac{4\pi}{\lambda} B_{23} sin(\theta - \alpha_{23}) + \frac{4\pi}{\lambda}\Delta\rho.
\end{aligned}$$

Note that if wc assume that Ap or $v\Delta T$ is constant (not an unreasonable assumption for ice sheet motion) during the multiple passes over the flow feature, the difference interferogram gives,

$$\Delta\phi'_{13} = \Delta\phi_{12} - \Delta\phi_{23}$$

$$= \frac{4\pi}{\lambda}(B_{12}sin(\theta - \alpha_{12}) - B_{23}sin(\theta - \alpha_{23})).$$

The contribution of the displacement field to the phase of the resultant interferogram, $\Delta\phi'_{13}$, has been removed . Resolving the individual baselines (B_{12}, B_{23}) into vertical, B^z, and horizontal, B^y, components gives,

$$\begin{aligned}
\Delta\phi'_{13} &= \frac{4\pi}{\lambda}((B^y_{12} - B^y_{23})sin\theta - (B^z_{12} - B^z_{23})cos\theta) \\
&= \frac{4\pi}{\lambda}(B^y_{13}sin\theta - B^z_{13}cos\theta) \\
&= \frac{4\pi}{\lambda}B_{13}sin(\theta - \alpha_{13})
\end{aligned}$$

which is equivalent to a topography-only interferogram observed with the baseline formed between the first and third passes. In other words, the sensitivity of the interferometer to topographic variation is now dependent on B_{13}. In the next section, wc will take advantage of this observation when we remove the topographic phase contributions to the interferograms.

The two mixed motion/topography interferograms ($\Delta\phi_{12}, \Delta\phi_{23}$) arc shown in Fig. 5. The interferogram, $\Delta\phi'_{13}$, formed from the difference between the interferograms A 4_{12} and A ϕ_{23} is shown also on the same figure. Since the topography is fairly smooth in this area (typically less than onc fringe), we color-coded the phase data a little differently to emphasize the subtle topographic variations. ~'here seem to be no residual motion fringes left in the difference fringe patterns. Indeed, wc compared this derived topographic map with the topographic map from differencing the $\Delta\phi_{23}$ and A ϕ_{34} interferograms and obtained almost identical results. The smaller spatial baseline B_{24} gave much noisier Observations. The gray scale image showing the relative topography is shown in Fig. 6. The elevation variation within that image is less that 150m. Again, wc emphasize that wc arc observing relative relief and to obtain absolute topography requires the presense of reference targets. Since observations of such small scale topographic variations arc not yet available over this ice feature, wc pm-form a qualitative check of the results. We created a simulated visible wavelength satellite image by illuminating the intcrfcromctrically-derived relief map and compared the results to an enhanced composite AVHRR image ['i'. Scambos, *Personal Communication]* of the same area. The similarity of the images is quite remarkable (Fig. 7). To emphasize the surface features, wc produced images which depict surf rface slopes (Fig. 8). We noticed high frequency spatial features superimposed on the smooth terrain. These features were not observed in the SAR intensity images. Again, wc observe these same features in the topographic map derived from $\Delta\phi'_{24}$. Without any surface observations, wc can only speculate on the nature of these features. It could be residuals duc to velocity variations in those areas which rendered our assumption] of constant velocity invalid. For this to be observed in both difference interferograms, the icc sheet will have to be accelerating or gradients in velocity in those areas. If that were the case, wc should treat the displacement as:

$$\Delta\rho = v\Delta T + a\Delta T^2$$

where a is the acceleration. An alternative explanation would be that they arc surface or subsurface features. If so, it is not clear why they arc not visible in the actual SAR images. At this time, wc do not have a satisfactory explanation for these possible artifacts.

5 Ice Sheet Motion without Topography

The removal of the topography-induced fringes is rather simple once wc have a digital elevation model of the region of interest. The general approach would be to create a synthetic topography-only interferogram with the correct baseline scaling and then subtract it from any arbitrary mixed motion/topography interferogram of the same area, This approach would entail an additional step of registering the elevation model to the geometry of the SAR data or vice versa. However, it would be relatively difficult to obtain fine registration between the datasets because visually well-deflncd features on the icc sheet arc almost IIol]-existent. Here, wc approach the problem a little differently by taking advantage of our co-registered datasets. Since wc have the topography-only interoferogram, $\Delta\phi'_{13}$, wc can now subtract it from the mixed interferogram formed with the first and third images (with 6-day separation), viz.

$$\Delta\phi_{13} - \Delta\phi'_{13} = \frac{4\pi}{\lambda}\Delta\rho$$

The result is a motion-only interferogram of the 6-clay relative displacement field. With this approach, wc have eliminated the steps of having to register the topography to the SAR data and of creating a synthetic topography-only interferogram. Fig. 9 shows the $\Delta\phi_{13}$ interferogram before and after the removal of topography. We attribute the 'Lull's eye' patterns in these mixed interferograms to ice motion over surface topography [2]. Wc observe, as expected, a reduction in the fringe density around the bull's eyes after the removal of the topography-induced fringe patterns. The source of the residual bull's eyes are discussed next.

in the presence of surface relief, the range-displacement or velocity (v_r) we observe is a function of the surface slope, ϕ, radar look angle, θ and the angle between the flow and look directions. The geometry is depicted in Fig. 10. If the unit vector whit}] defines the radar look vector is $\vec{r} = (0, \sin\theta, -\cos\theta)$, and the actual icc motion vector is $\vec{v} = v(\cos\phi\sin\xi, \cos\phi\cos\xi, \sin\phi)$, then the interferometric ally-observed velocity is the projection of the motion vector into the range look direction,

$$v_r = \vec{v} \cdot \vec{r} = v(\cos\phi\cos\xi\sin\theta - \sin\phi\cos\theta)$$

ξ is the angle (in they --z plane) between the flow direction and the look direction, and the surface slope is in the direction of the flow. The implicit assumption is that the flow vector is tangent to the surface topography. Wc also note that $v\cos\phi$ and $v\sin\phi$ arc the horizontal and vertical components of the velocity vector in the flow direction and that the second term in the equation is independent of ξ. Wc see from this equation that the interferometrically-derived motion has contributions from both components. The relative contribution of the two terms to v_r is *given* by their ratio: $\mathcal{R} = \cot\phi\tan\theta\cos\xi$. For $\phi =$ 5", $\theta = 23°$ (ERS-1) and $\xi = 30°$; this ratio is approximately 4. So, even for relatively small surface slopes the contribution of the second term is quite significant. It is therefore important to realize that there is a mixing of the vertical and horizontal components in the observed velocity. Conversely, if the three angles (ϕ, O, ξ) are available then we can easily compute the fractional contribution of the components. O is a system parameter and ϕ can be derived from the relief map constructed from the interferometric technique described here. If wc have some idea of the flow direction, such as requiring flow to be parallel to the margins of the ice stream, we can estimate this ratio. Errors in computing this ratio are given by its partial relative to ξ,

$$\frac{\partial \mathcal{R}}{\partial \xi} = -cot\phi tan\theta sin\xi.$$

The errors would be high if ξ is large because the interferometric system is less sensitive to horizontal motion as the angle ξ approaches $\pi/2$.

6 Description of Flow Field

The velocity field shown in Figure 8 reflects the localized big}] flow speed in the ice stream. Ice flows from the lower left to the upper right in the figure. On the left (upstream), the margins on either side of the stream are clearly the areas of highest shear strain, with the interior ice moving $\approx$ 30 m/yr faster in the interior than at the edge.]n the right of the figure (downstream), the flow has accelerated dramatically, reaching velocities of more than 100 m/yr. The nature of the margins has also changed, with the shear occuring in a broad region across the stream, rather than being concentrated at the margins. This change in the character of the flow in less than 100 km is remarkable, and may reflect a fundamental change in the mechanics responsible for the motion. in glaciological terms, it is a transition from plug flow to flow with a more parabolic velocity profile.

'7 Discussion

Here, we have described the procedures used to derive high-resolution relief and ice motion maps using multiple-pass radar interferometry. We summarize our approach here. First, we use differential interferometry to remove the phase contribution of the displacement field to obtain a topography-onl y interferogram. Then], we subtract this topography-only interferogram from the mixed interferograms to separate the displacement fringe patterns from those due to relief. 'l'he important underlying assumption is that the ice motion field remains coxkstant over the period of observation. Indeed, for the flow feature we studied in this paper, this assumption seems valid. If there are snort term flow variations, there will be mixing of the topographic, fringes and motion fringes in the results. Care should be exercised in interpreting such results.

We also emphasize that we have not derived absolute topography or motion, only their relative measurements, The use of surface targets as elevation or motion references cannot be approached using the traditional way of tiepoint identification; both because there are few well-defined natural features and because those that exist move with the ice. Since the ice sheet surface slopes (large sc.ale) are small (1 in 1 00), the error in relief due to spatial misregistration between a reduced-resolution interferogram and a low-resolution digital elevation model (DEM) should be small. We could scale the interferometric DEM to laser altimetry flight lines or level lines produced by field parties. Ice motion could be referenced to a corner reflector with a velocity measured by GPS survey. Of course, exposed bedrock would be useful for such purposes too.

For ice flow velocity monitoring, there is an obvious limit on the highest velocity which can be detectable with an interferometric system. over this limit, the phase is impossible to unwrap. Wc usc the maximum spatial gradient of the velocity to define this limit,

$$\delta_v = \frac{\lambda}{2\beta_r \Delta T sin\theta}$$

where λ is the wavelength and β_r is the ground resolution of the multi-look or averaged data. Assuming that the data is sampled correctly, the detectability is inversely proportional to the resolution and the time separation. Using the three-day repeat frequency of ER - 1 and a ground range resolution of 100n1 (after some averaging process), this limit is approximately 10-5/clay. In other words, over a distance of one kilometer the velocity difference which can be detected is roughly 1 cm/day or 3.65 In/year. Over this limit, tracking ice features in sequential remote sensing images would be more appropriate. For slow icc motion, the system parameters which limit observation arc phase noise and temporal baseline. Temporal decorrelation of the scattering surface would limit the usc of observations with long time separations.

The prospect of using multiple-pass radar interferometry to obtaining high resolution topography and motion for monitoring ice sheets is promising, with the expected launch of RADARSAT and ERS-2 in the next few years. These active microwave sensors are not dependent on solar illumination or limited by clouds. Presently, we are limited to observing motion along the line of sight of the radar. With a more extensive dataset, we can measure the horizontal field of velocity by compositing motion observations from ascending and descending orbits.

Acknowledgments

R. Kwok and C. Chan performed this work at the Jet Propulsion laboratory, California Institute of Technology under contract with the National Aeronautics and Space Administration. M. Fahnestock performed this work as a USRA visiting fellow at the Goddard Space Flight Center.

References

1. Goldstein R. M., 11. Engelhardt, B. Kamb, R. M. Frolich, Satellite radar Interferometry for monitoring ice sheet motion: Application to an Antarctic Ice Stream, Science, Vol. 262, pp. 1525-1530,1993.

2. Joughin, 1. R., D. 1'. Winebrenner and M.A. Fahnestock, Observations of Complex Ice-Sheet Motion in Greenland Using Satellite Radar Interferometry. Submitted to *Nature.*

3. Fahnestock, M., R. Bindschadler, R. Kwok and K. Jezek, Greenland Ice Sheet Surface Properties and Ice Dynamics from 131/S-1 Synthetic Aperture Radar Imagery, *Science*, vol. 262, 1530-1534, 1993.

4. Zebker, 11. and R. Goldstein, Topographic mapping from interferometric SAR observations, *J. Geophys. Res.*, Vol. 91, No. B5, pp. 4993-4999, 1986.

5. Goldstein, R., 1 I. A. Zebker and C. Werner, Satellite radar interferometry: Two-dimensional phase unwrapping, *Radio Sci.*, Vol. 23, No. 4, pp. 713-720, 1988.

6. Li, F. and R. M. Goldstein, Studies of multi-baseline interferometric synthetic aperture radars, *IEEE Trans. Geosci. Remote Sens.*, Vol, 28, pp. 88-97, 1990.

7. Rodriguez, E. and J. Martin, Theory and design of interferometric SARs, *Proc. IEE* Vol.139, No. 2, 1990.

8. Zebker, 11. A., C. 1,. Werner, P. A. Rosen, S. Hensley, Accuracy of topographic maps derived from ERS-1 interferometric radar, *IEEE Trans. Geosci. Remote Sens.*, Vol, 32, pp. 823-836, 1994.

9. Gabriel, A. K., R. M. Goldstein and 11. A. Zebker, Mapping small elevation changes over large areas: Differential radar interferometry, *J. Geophys. Res.*, Vol. 94, No. B7, pp. 9183-9191, 1989.

10. ERS-1 FRINGE: SAR Interferometry Orbit Listing. ESRI N/ESA Missions Section.

11. Gabriel, A. 1{. and R. M. Goldstein, Crossed orbit interferometry: Theory and experimental results from SIR-B, *Int. J. of Remote Sins.*, Vol. 9, No. 8, pp. 857-8'72, 1988.

Table 1

ERS-1 IMAGE SEQUENCE (Identification and Date of Acquistion)

Image No.	Orbit/Frame Number	Date Acquired
1	12886/1557	1-Jan-1994
2	12929/1557	4-Jan-1994
3	12972/1557	7-Jan-1994
4	13015/1557	10-Jan-1994

Table 2

Approximate Baselines, B_{ij} at 23° Look Angle (meters)

Between Images (i, j) in Table 1 [10]

Baseline	$B_{\parallel}$	$B_{\perp}$
B_{12}	23	59
B_{13}	50	8
B_{14}	45	-14
B_{23}	27	-53
B_{24}	22	-75
B_{34}	-5	-21

Figure Captions

Figure 1. Location of ERS-1 SAR images and flow feature on Greenland.

Figure 2. Interferometer imaging configuration, A baseline, B, is created between the ith and jth repeat observations of the same ground area. At an almost identical look angle of θ, the differential range to a point on the ground is given by the interferometric phase. α is the tilt of the baseline relative to the horizontal.

Figure 3. ERS-1 SAR images of the flow feature in northeast Greenland. (a) Image 1 (12886/1 557). (b) image 2 (12929/1 557) (©ESA 1994).

Figure 4. Three interferograms, $\Delta\phi$, formed from the 4 images. (a) $\Delta\phi_{12}$, interferogram formed from images 1 ant] 2 in Table 1, the observations are separated by 3 days. (b) $\Delta\phi_{13}$, the observations are separated by 6 days. (c) $\Delta\phi_{14}$, the observations arc separated by 9 days. The color fringes show the relative changes in topography of the ice sheet as w c]] as relative motion of the ice in the range (line of sight) direction of the radar. The fringes due to topography is dependent on the baseline. For motion, one fringe represents a 2.8 cm movement relative to the spacecraft.

Figure 5. Differencing of the interferograms $\Delta\phi_{12}$ and $\Delta\phi_{23}$. (a) $\Delta\phi_{12}$. (b) $\Delta\phi_{23}$. (c) $\Delta\phi'_{13}$, the differential interferogram shown with the displacement field removed. The phase variation is emphasized in this representation. Each cycle of the color wheel represents a $\pi/2$ instead of 2π phase shift as in the interferograms in the other figures. As a result, the phase noise is more pronounced.

Figure 6. Gray scale representation of the topography. The range of topographic variations is less than 150m.

Figure 7. Comparison of illuminated topography with AVHRR image of the same area, (a) Illuminated topographic map derived from differential interferometry. (b) AVHRR image of

the same area.

Figure 8. Map of surface slopes. (a.) Derived from $\Delta\phi'_{13}$. (a) Derived from $\Delta\phi'_{24}$.

Figure 9. Removal of topographic phase from $\Delta\phi_{13}$. (a) $\Delta\phi_{13}$, mixed motion/topography interferogram. (b) $\Delta\phi_{13}$ - $\Delta\phi'_{13}$, motion only interferogram.

Figure 10. Effect of surface relief on observed line of sight velocity,

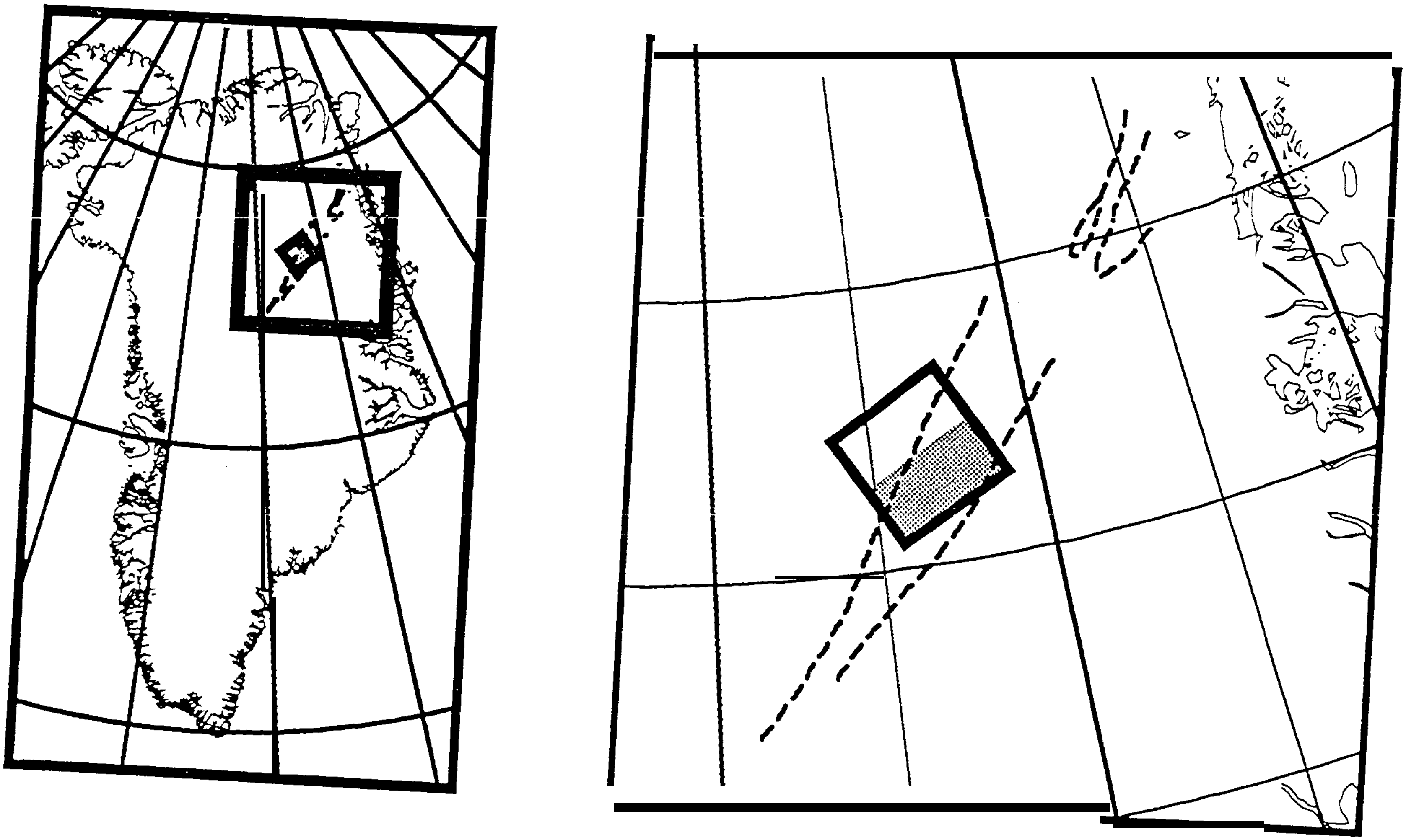

FIG 1

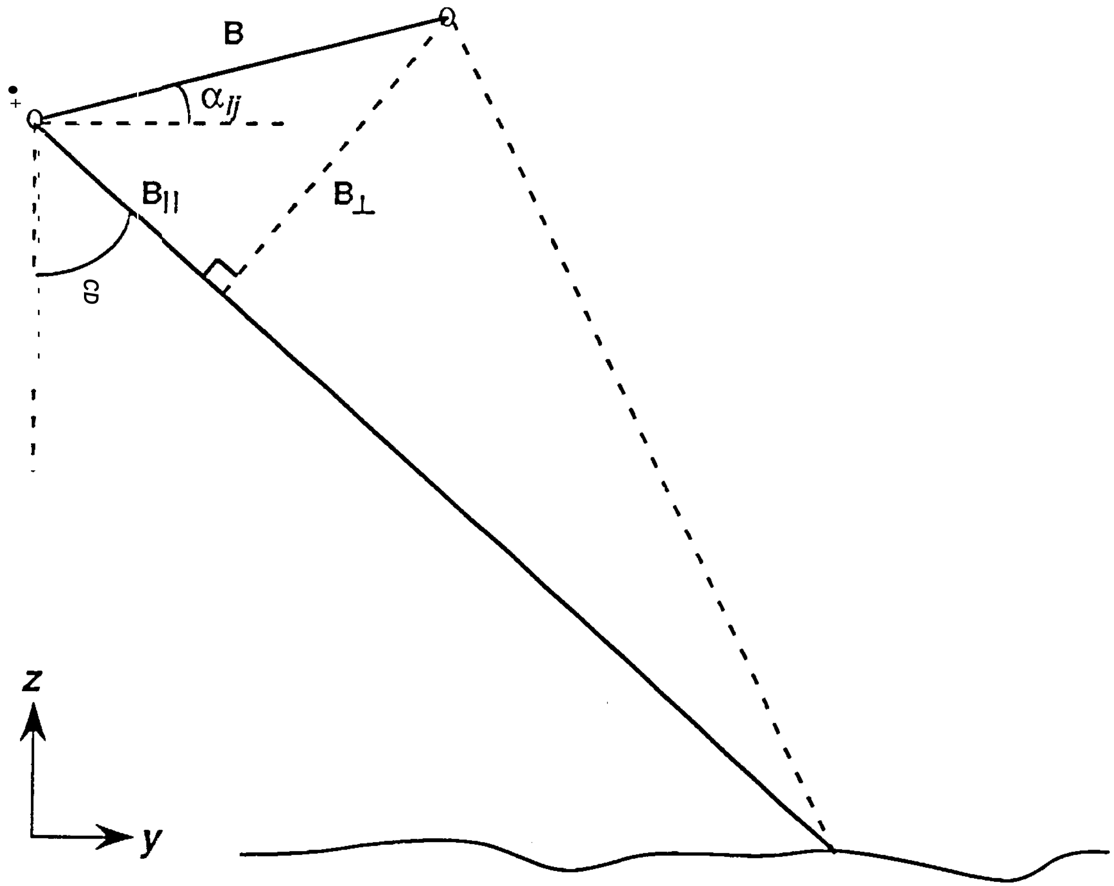

Fig. 2

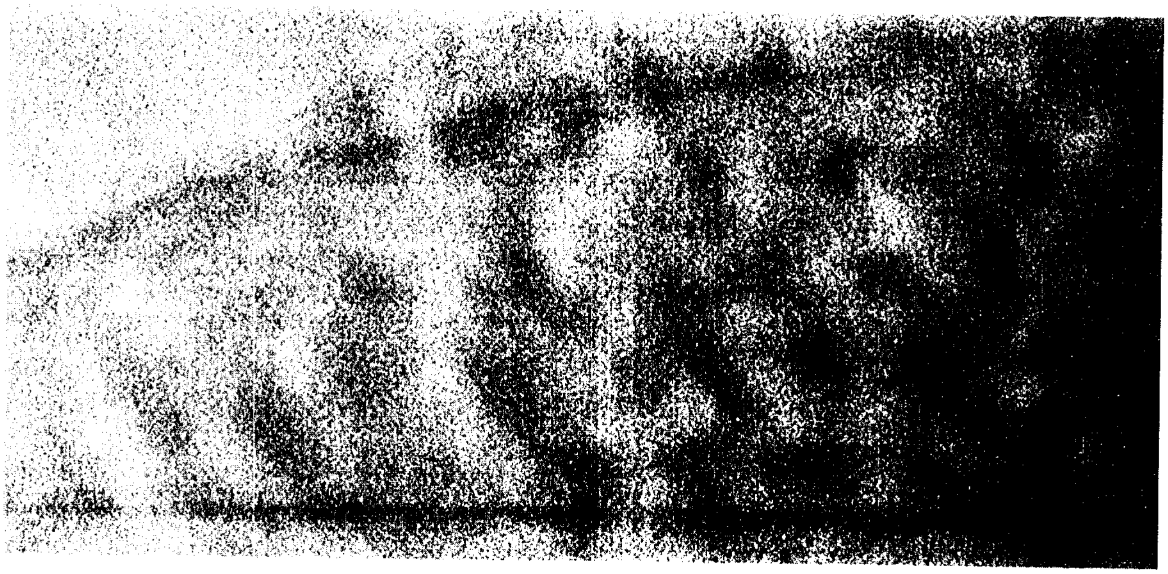

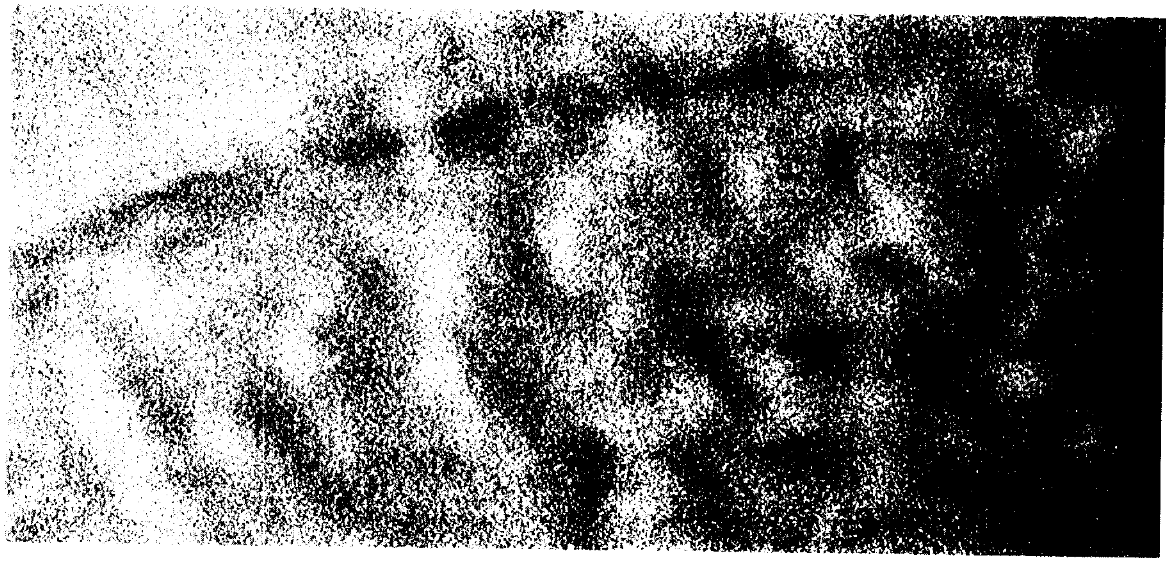

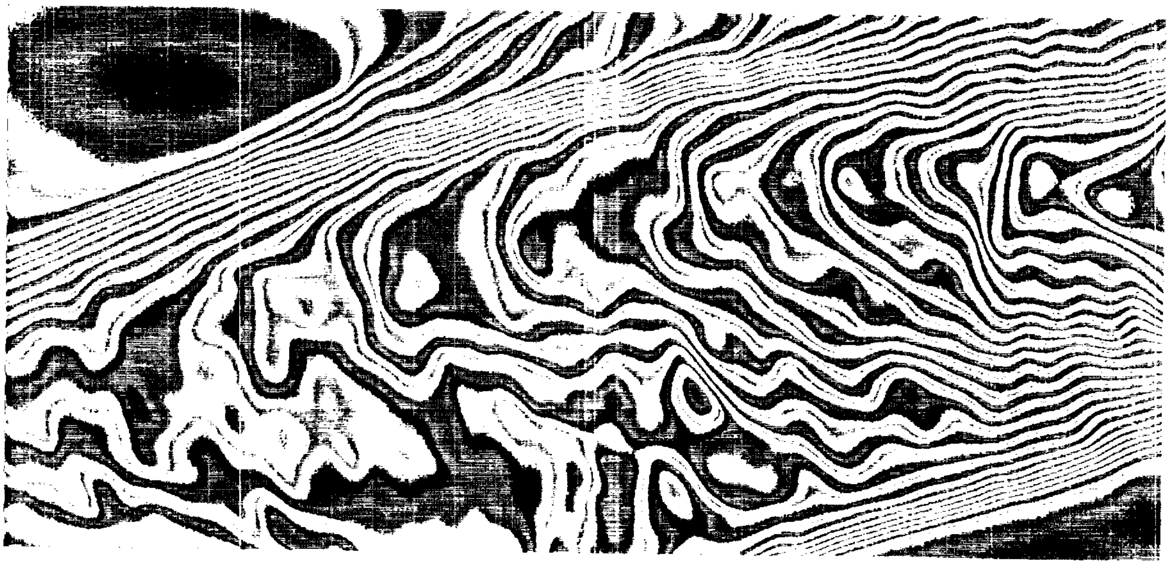

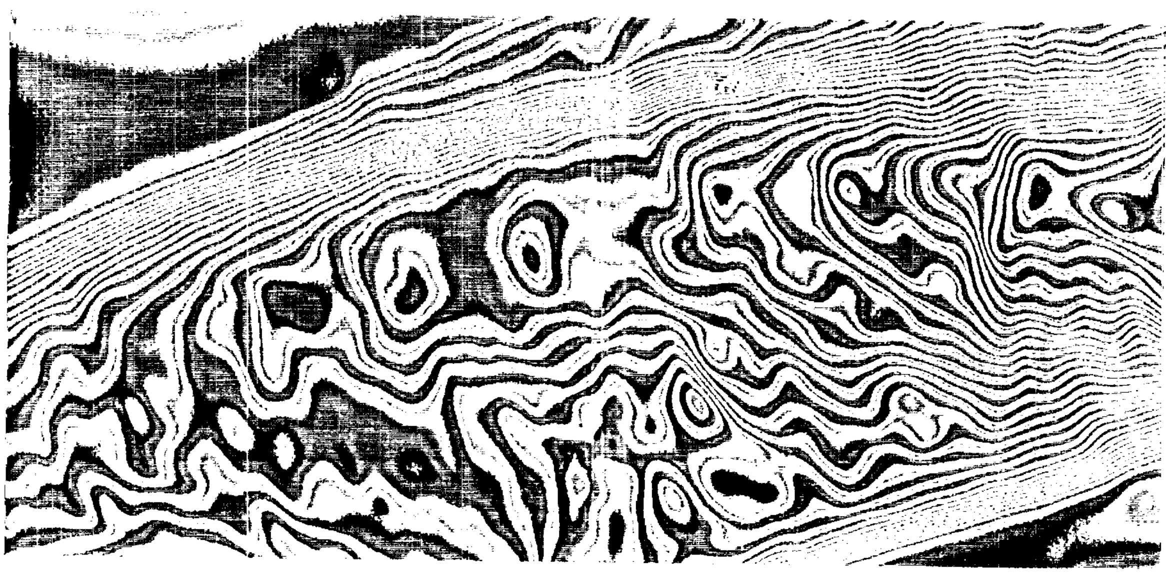

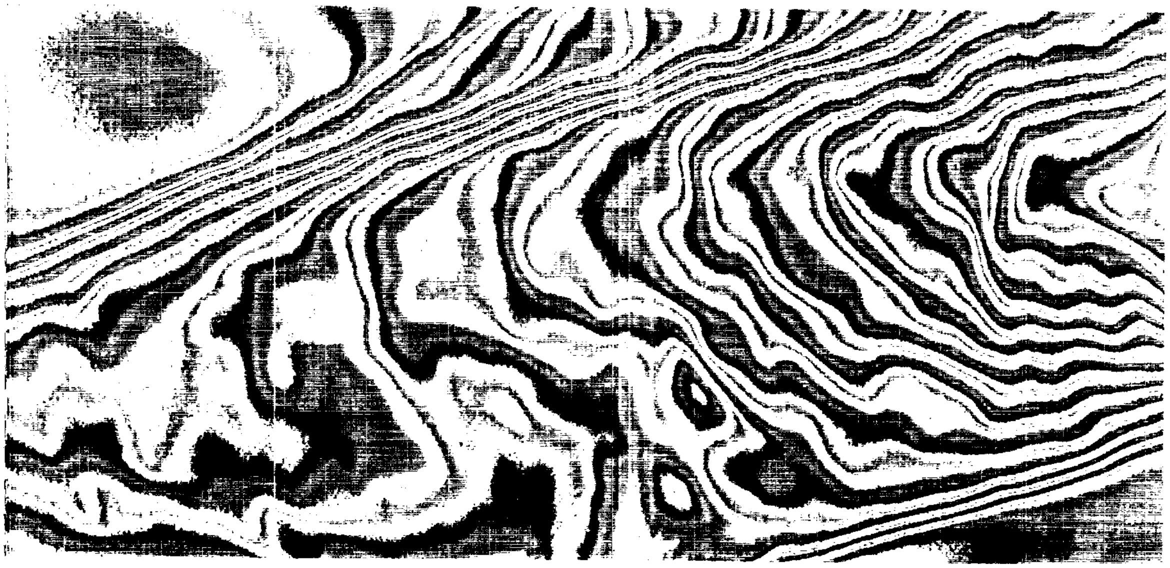

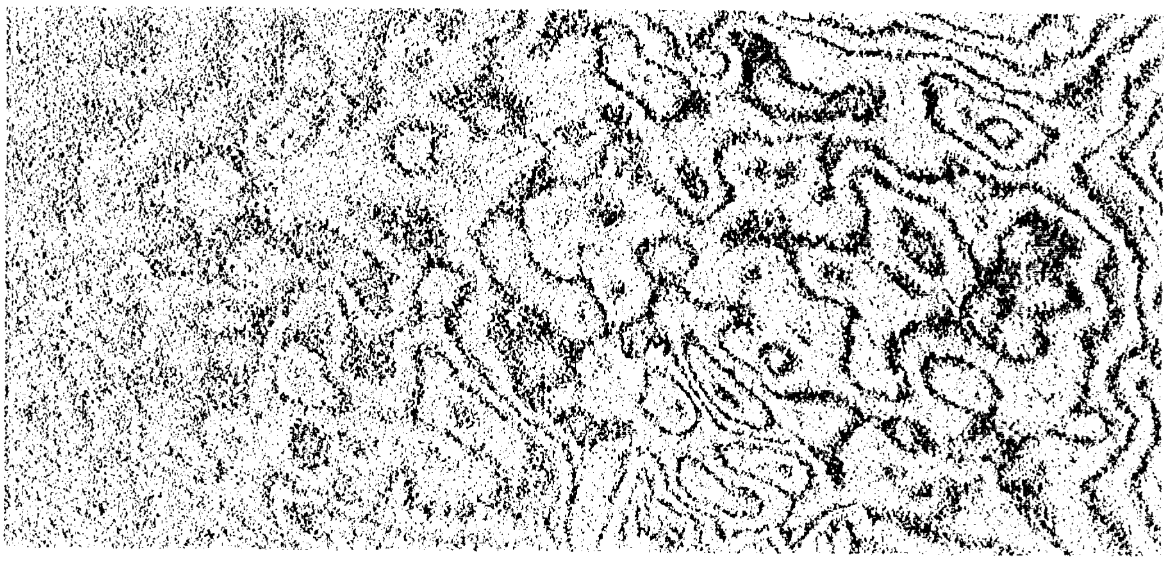

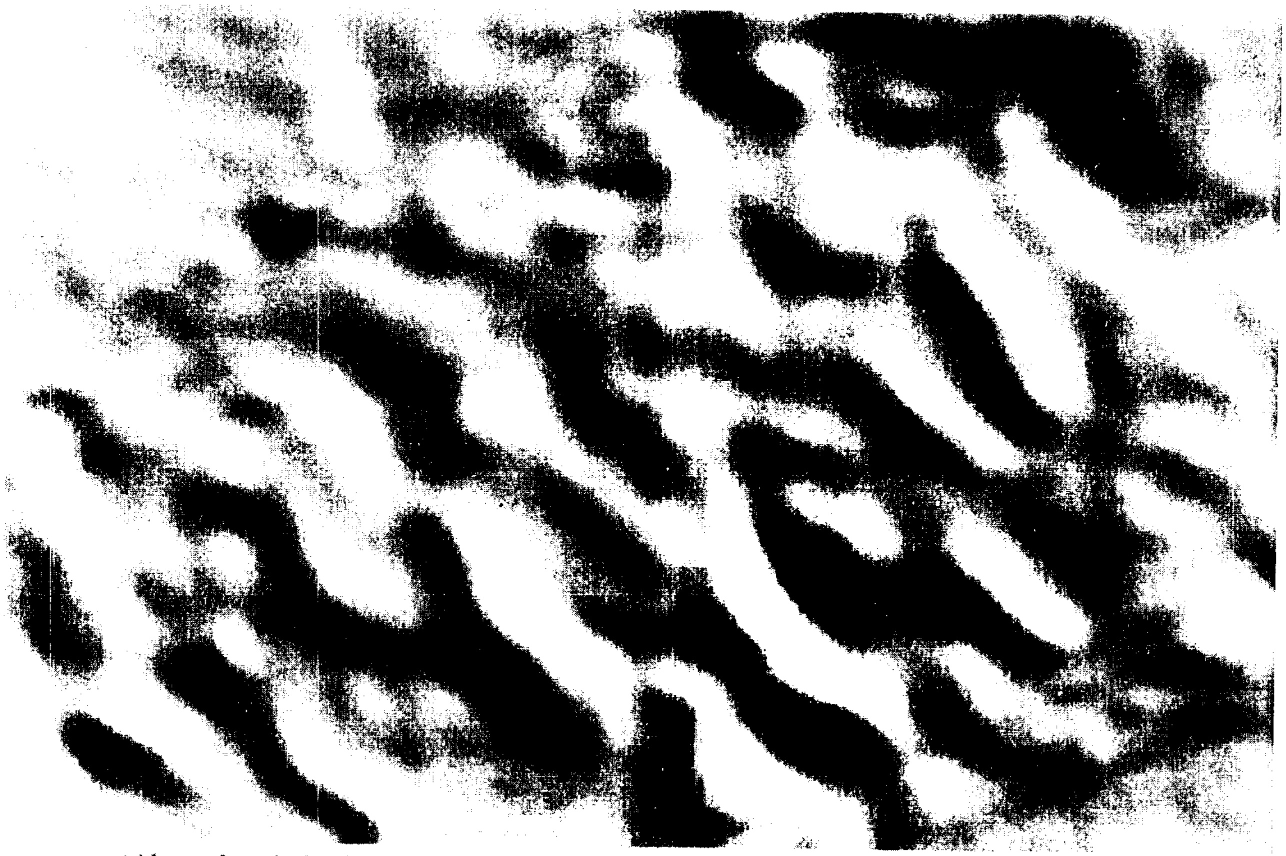

Shaded DEM derived from two interferograms

Enhanced AVHRR band 2 image

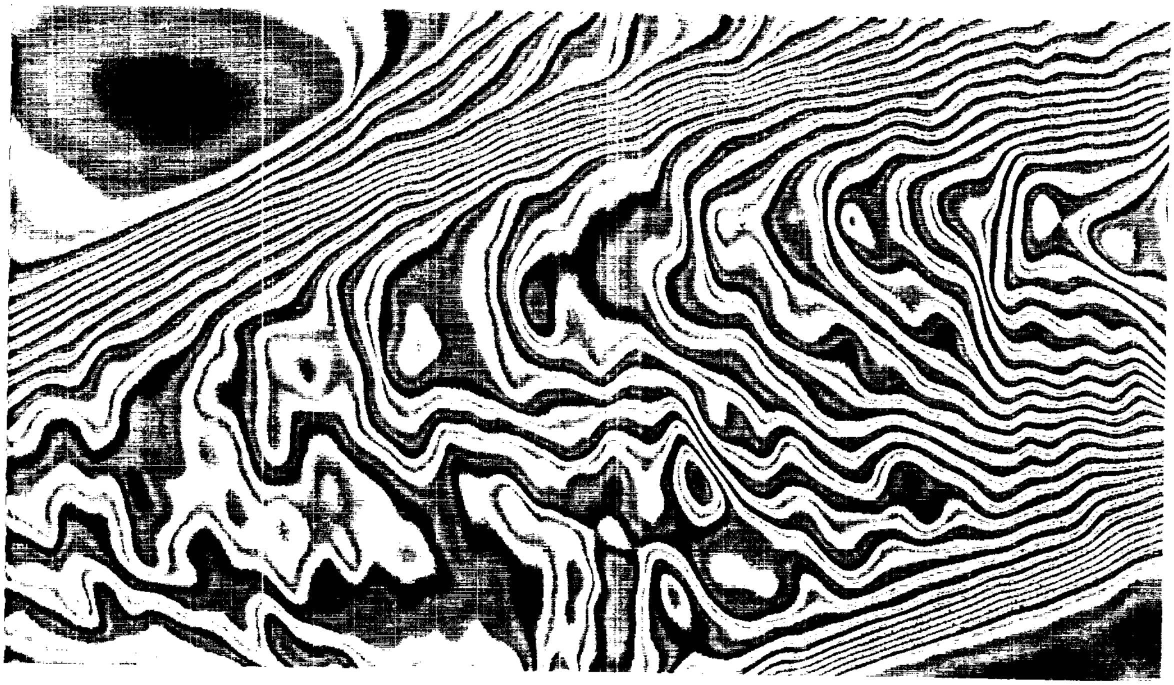

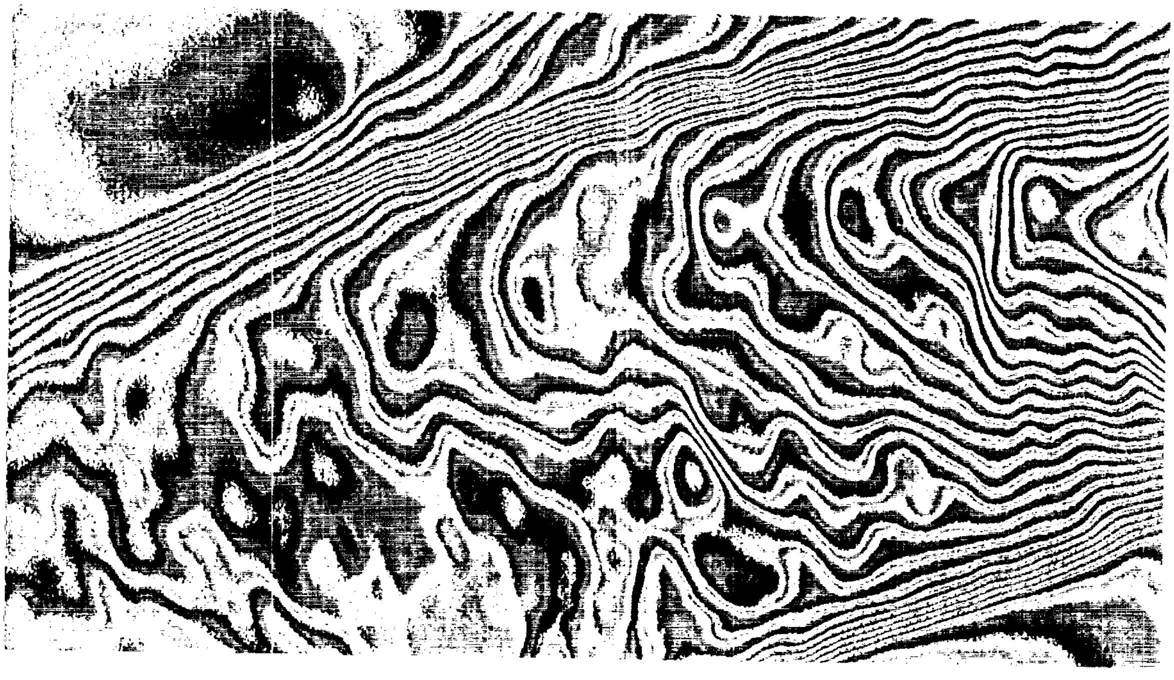

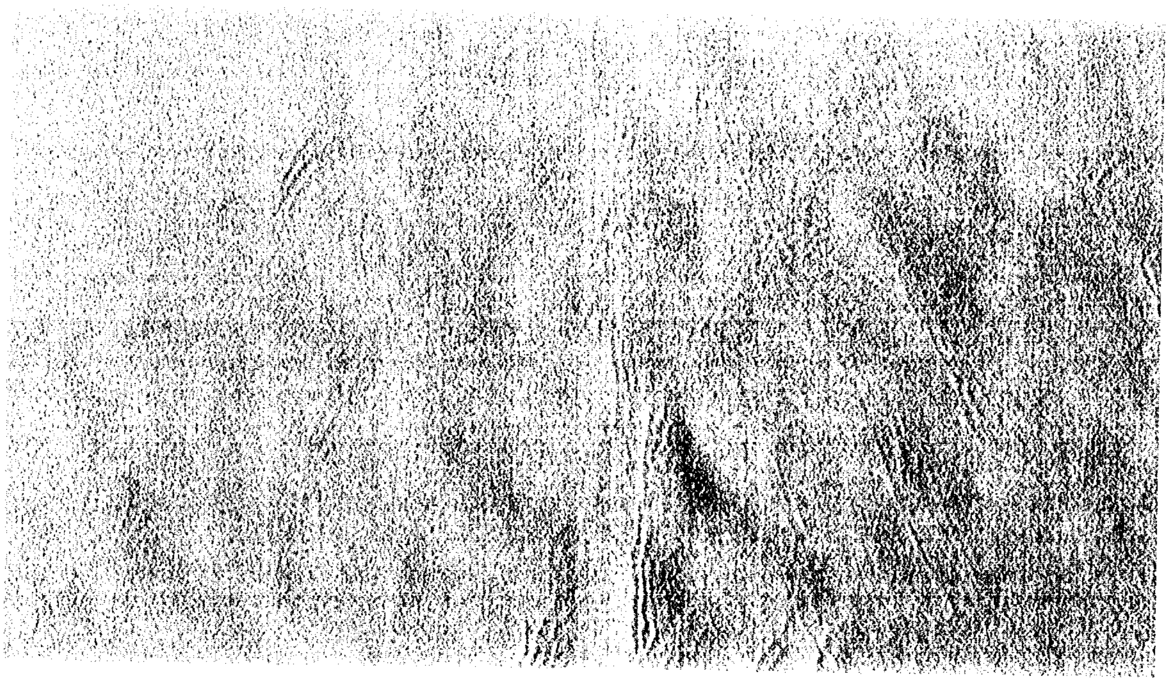

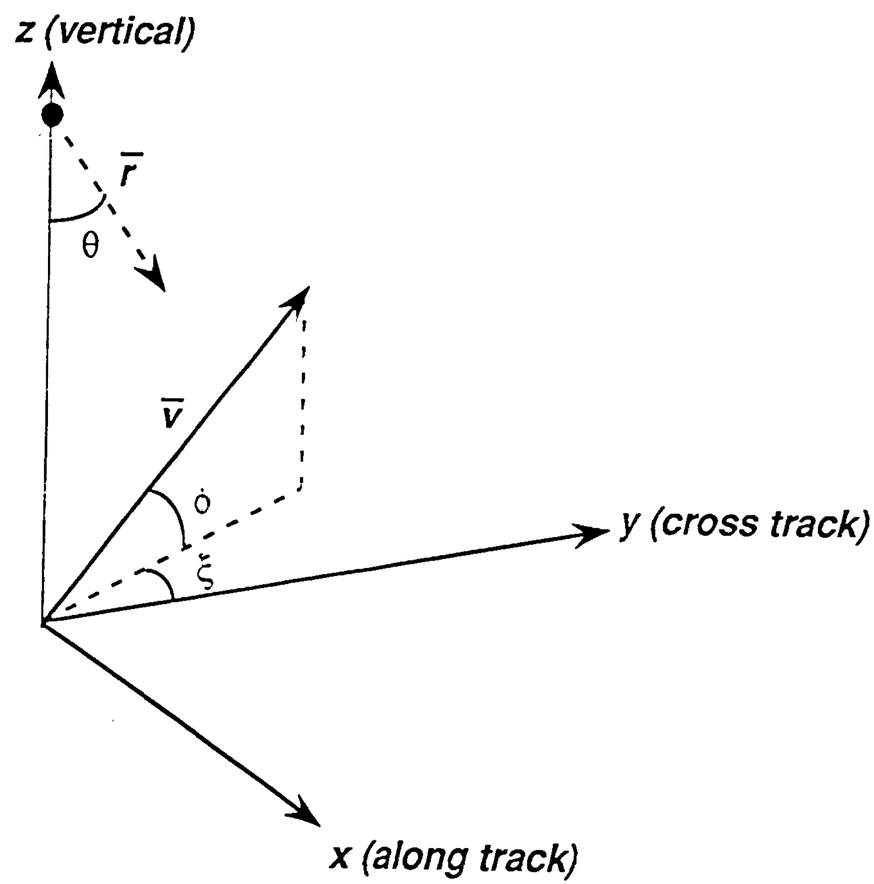

Fig. o